Explicit expression of mesophyll conductance in the traditional leaf photosynthesis–transpiration coupled model and its physiological significances

Hong Luo[1], Marc Carriquí[2], Miquel Nadal[2], Tuo Han[3], Christiane Werner[4], Jian-feng Huang[5], Jiao-lin Zhang[5], Zhi-guo Yu[6], Feng-min Li[1], Xiang-wen Fang[1], Wei Xue[1*]

[1]Department of Ecology and Environmental Sciences, School of Life Sciences, State Key Laboratory of Grassland Agro-ecosystems, Lanzhou University, Lanzhou 730000, China

[2]Research Group in Plant Biology under Mediterranean Conditions, Agro-Environmental and Water Economics Institute, Universitat de les IllesBalears, Palma, IllesBalears 07122, Spain

[3]The Northwest Institute of Eco-Environment and Resources, Chinese Academy of Sciences, Lanzhou 730000, China

[4]Department of Ecosystem Physiology, University of Freiburg, Freiburg 79110, Germany

[5]Key Laboratory of Tropical Forest Ecology, Xishuangbanna Tropical Botanical Garden, Chinese Academy of Sciences, Mengla 666303, China

[6]Nanjing University of Information Science and Technology, School of Hydrology and Water Resources, Nanjing 210044, China

*Author for correspondence: Wei Xue, Tel: 0931-8912560; Email: xuewei@lzu.edu.cn

Total word count (excluding summary, references and legends):	6475	No. of figures:	4 (all of Fig in color)
Summary:	189	No. of Tables:	2
Introduction:	888	No. of Supporting Information files:	16 (Figs. S1–S10; Tables S1–S6)
Materials and Methods:	1798		
Results:	1657		
Discussion:	2132		

Explicit expression of mesophyll conductance in the traditional leaf photosynthesis–transpiration coupled model and its physiological significances

Summary

- Almost all terrestrial biosphere models (TBMs) still assume infinite mesophyll conductance (g_m) to estimate photosynthesis and transpiration. This assumption has caused low accuracy of TBMs to predict leaf gas exchange under certain conditions.
- In this study, we developed a photosynthesis–transpiration coupled model that explicitly considers g_m and designed an optimized parameterization solution through evaluating four different g_m estimation methods in 19 C_3 species at 31 experimental treatments.
- Results indicated that temperature responses of the maximum carboxylation rate (V_{cmax}) and the electron transport rate (J_{max}) estimated by fusing the Bayesian retrieval algorithm and the Sharkey online calculator together with g_m temperature response estimated by fusing the chlorophyll fluorescence–gas exchange method and anatomy method predicted leaf gas exchange more accurately. The g_m temperature response exhibited activation energy (ΔH_a) of 63.13 ± 36.89 kJ mol^{-1} and entropy (ΔS) of 654.49 ± 11.36 J K^{-1} mol^{-1}. The g_m optimal temperature (T_{opt_gm}) explained 58% of variations in photosynthesis optimal temperature (T_{optA}). The g_m explicit expression has equally important effects on photosynthesis and transpiration estimations.
- Results advanced understandings of better representation of plant photosynthesis and transpiration in TBMs.

Keywords: mesophyll conductance, photosynthesis, terrestrial biosphere models, temperature response, transpiration

Introduction

The leaf photosynthesis–transpiration coupled model is the basis of vegetation photosynthesis and transpiration estimations performed using terrestrial biosphere models (TBMs) (Dai *et al*., 2003; Rogers *et al*., 2017). The model is based on the biochemical-based photosynthesis theory developed by Farquhar *et al*. (1980), which considers the leaf stomatal aperture as the primary gauge of CO_2 influx and water vapor efflux and assumes an infinite conductance of CO_2 diffusion from sub-stomatal cavities to the chloroplast stroma (i.e. mesophyll conductance, g_m). In such cases, there is no CO_2 concentration drawdown between the intercellular airspace and the chloroplast stroma. However, now it is widely accepted not only that there is a significant CO_2 diffusion drawdown from the intercellular airspace to the chloroplast stroma, but that the resistance that causes this drawdown can be similar or greater than stomatal resistance in land plants (Flexas *et al*., 2012; Evans and von Caemmerer, 2013; von Caemmerer and Evans, 2015; Gago *et al*., 2019). Currently, almost all TBMs do not explicitly consider g_m (Rogers *et al*., 2017; Knauer *et al*., 2019; 2020; Iqbal *et al*., 2021), primarily because of (1) huge disputes in response characteristics of g_m to ambient environment, particularly the temperature response (von Caemmerer and Evans, 2015; Bahar *et al*., 2018; Shrestha *et al*., 2019; Li *et al*., 2020; Evans, 2021), and (2) lack of a g_m finite photosynthesis–transpiration coupled model that can be applied to as many C_3 species as possible (Niinemets *et al*., 2009; Xue *et al*., 2017; Knauer *et al*., 2020).

Mesophyll conductance cannot be directly measured mainly because it is not possible to determine the CO_2 concentration within the chloroplast stroma. Thus, modeling methods are required to estimate g_m, which could be grouped into four classes according to the algorithm principle and field measurement tools: the chlorophyll fluorescence–gas exchange method (i.e. g_{m_F}) (Harley *et al*., 1992); the anatomy method (i.e. g_{m_A}) (Tosens *et al*., 2012; Tomas *et al*., 2013); the ^{13}C isotope discrimination method (Evans *et al*., 1986; Barbour *et al*., 2007; Pons *et al*., 2009; Evans and von Caemmerer, 2013; Flexas *et al*., 2013); and the curve-fitting parameter

retrieval methods (Sharkey *et al*., 2007; von Caemmerer *et al*., 2009; Yin and Struik, 2009; Gu *et al*., 2010; Zhu *et al*., 2011; von Caemmerer, 2013, Han *et al*., 2020; Xiao *et al*., 2021). These methods have their own advantages and weakness in terms of model parameter assumptions made during estimation, resulting in large discrepancies in the estimated temperature response of g_m (Pons *et al*., 2009; Evans, 2021). Therefore, we decided to select the best g_m estimation method in terms of accuracy in predicting leaf gas exchange at any temperature, namely a good criterion to select at each temperature which g_m estimation method works best is the one that could predict leaf gas exchange more accurately.

Effects of the g_m finite expression on photosynthesis have been widely demonstrated, whereas few attentions are paid on transpiration. Considering the indirect effects of g_m on transpiration and the direct effect on photosynthesis through its control on chloroplast CO_2 concentration, Knauer *et al*. (2020) determined that g_m has a greater effect on photosynthesis but no significant effects on transpiration in most species and hence proposed the 'the asymmetric effects on photosynthesis and transpiration estimations' hypothesis. Kumarathunge *et al*. (2019) found that variations in photosynthesis optimal temperature (T_{optA}) can be primarily explained by changes in the ratio of the apparent maximum electron transport rate and the apparent maximum carboxylation rate at 25°C ($J_{a,25}/V_{a,25}$, JVr), thus proposing 'the JVr biochemical limitations' hypothesis. $J_{a,25}$ and $V_{a,25}$ estimations in their study were derived from the A_n/C_i curve without explicitly considering g_m. Previous results indicated significant changes in T_{optA} under different intercellular CO_2 concentrations (C_i) in C_3 species (Farquhar *et al*., 1980; Rogers *et al*., 2017), suggesting that the CO_2 substrate levels significantly affect T_{optA}. The CO_2 substrate levels inside the chloroplasts in turn are strongly controlled by g_m. We speculated that the plausibility of the T_{optA}–JVr relationship reported by Kumarathunge *et al.* (2019) is questionable in reality. The observed variations in T_{optA} among plant species may not be solely explained by biochemical limitations.

As a first step towards the better representation of plant photosynthesis and

transpiration in most TBMs, we attempted to develop a g_m finite model that could be directly implemented in most TBMs, in addition to design an optimized parameter configuration solution that is physiologically meaningful for as many C_3 species as possible. The optimized parameterization solution was designed by comparing multiple different parameter estimation methods used for g_m, V_{cmax}, and J_{max} estimations. The response features of g_m, V_{cmax}, and J_{max} to temperature were therefore determined. Dynamic changes in apparent g_m in response to irradiance were not of main consideration in the current study, since the underlying conductance at the cellular level may remain unchanged with varying light environments (Evans, 2021). Validation of the predictability of the g_m finite model compared to a traditional photosynthesis model assuming infinite g_m (abbreviated as the g_m infinite model) was performed in 19 C_3 species under 31 experimental conditions. The effects of the g_m finite expression on leaf photosynthesis and transpiration estimations were quantified to evaluate the 'the *JV*r biochemical limitations' hypothesis proposed by Kumarathunge *et al*. (2019) and 'the asymmetric effects on photosynthesis and transpiration estimations' hypothesis proposed by Knauer *et al*. (2020).

Materials and methods

Model description

In line with the photosynthesis–transpiration coupled model adopted by most TBMs, the Farquhar, von Caemmerer & Berry (1980) (FvCB) photosynthesis model and a stomatal conductance sub-model (Ball *et al*., 1987; Leuning, 1995) were coupled to quantify leaf carbon uptake and water loss through transpiration. A_n is limited either by the Rubisco carboxylation rate at a low CO_2 concentration (W_c) or the RuBP regeneration rate at a relatively high CO_2 concentration because of low electron transport rates (W_j) or deficit inorganic phosphate for photophosphorylation (W_p). A_n can be expressed as follows:

$$A_n = \left(1 - \frac{\Gamma^*}{C}\right) \min\{W_c, W_j, W_p\} - R_d \qquad \text{(Eqn 1)}$$

$$W_c = \frac{V_{cmax}C}{\mathrm{C} + K_c(1 + O/K_o)} \quad \text{(Eqn 2)}$$

$$W_j = \frac{JC}{4(\mathrm{C} + 2\Gamma^*)} \quad \text{(Eqn 3)}$$

$$W_p = 3TPU \quad \text{(Eqn 4)}$$

where V_{cmax} is the maximum carboxylation rate; Γ^* is the CO_2 compensation point without mitochondrial respiration; K_c and K_o are the Michaelis–Menten constants for CO_2 and O_2, respectively; R_d and J are dark respiration in the light and the electron transport rate, respectively; *TPU* is the rate of triose phosphate export from the chloroplasts. C is C_i for the g_m infinite model or CO_2 concentration inside the chloroplasts (C_c) for the g_m finite models, which can be determined using Eqns. 9 and 10. J is modeled as a function of incident photosynthetically active radiation (*PAR*), which is calculated using the non-rectangle hyperbola equation (Eqn. 5) (Farquhar *et al*., 1980; Medlyn *et al*., 2002; Sharkey *et al*., 2007; Rogers *et al*., 2017; Kumarathunge *et al*., 2019) as follows:

$$\Theta J^2 - (\alpha PAR + J_{\max})J + \alpha PAR J_{max} = 0 \quad \text{(Eqn 5)}$$

where α is the quantum yield of electron transport; Θ is the curvature of the non-rectangle hyperbola equation (Table 1).

Under well-watered conditions, the correlation between photosynthetic parameters and temperature can be expressed by the peak Arrhenius function (Dreyer, 2001; Medlyn *et al*., 2002; Xue *et al*., 2017; Kumarathunge *et al*., 2019; Knauer *et al*., 2019) as follows:

$$V_{c_{max}}/J_{max}/g_m = \frac{k_{25}e^{\Delta H_a(T_k-298.1)/298.1/R/T_k}}{1 + e^{(\Delta S T_k - \Delta H_d)/R/T_k}}(1 + e^{(298.1\Delta S - \Delta H_d)/R/298.1}) \quad \text{(Eqn 6)}$$

where k_{25} is the photosynthetic parameter value at 25°C ($V_{cmax,25}$, $J_{max,25}$, or $g_{m,25}$); ΔH_a is the activation energy; ΔH_d is the deactivation energy; ΔS is the entropy term which characterizes the changes in reaction rate caused by substrate concentration (Table 1); T_k is leaf temperature in Kelvin unit; and R is the gas constant (8.314 Pa m^3 K^{-1} mol^{-1}).

V_{cmax}, J_{max}, and g_m can be estimated from field measurements, whereas C remains unknown in the leaf photosynthesis model. The leaf photosynthesis model is therefore

required to be coupled with the stomatal conductance sub-model for predicting the behavior of stomatal conductance by depending on environmental drivers and A_n. The stomatal conductance sub-model can be expressed as follows:

$$g_{sw} = g_{min} + g_{fac}\frac{A_n}{(C_s - \Gamma^*) \times \left(1.0 + \frac{VPD}{a}\right)} \quad \text{(Eqn 7)}$$

where C_s is leaf surface CO_2 concentration; a is a constant (default as 35kPa); g_{min} is the value of g_{sw} when A_n is zero; g_{fac} is the stomatal sensitivity to the assimilation rate; and *VPD* is the vapor pressure deficit between the leaf surface and atmosphere; g_{sw} is the stomatal conductance to water vapor; and g_{fac} and g_{min} are the slope and intercept of the linear relationship between g_{sw} and A_n, respectively, which were extracted from the diurnal gas exchange data.

To predict the response of A_n to leaf temperature at ambient and relatively high CO_2 concentrations and light saturation levels (i.e. A_{max}–T_{leaf} curve) for the species derived from literature, we needed to determine the g_{fac} and g_{min} values, without the diurnal gas exchange information. According to our field measurements, g_{fac} was set to 3.0 for the woody species and 4.0 for the herbaceous species. The g_{min} was set to 10.0 mmol m^{-2} s^{-1} for both C_3 woody and herbaceous species, as commonly adopted by most TBMs (Sellers *et al*., 1996). An initial value was set for *C*, and then, A_n was determined using Eqn. 1. The known A_n was substituted into Eqn. 7 for g_{sw} estimation, which in turn was substituted into Eqn. 8 or 9 to generate a new *C* value. The new *C* value was then compared with the previous value. This new *C* value was adjusted and then considered as the second initial value for Eqn. 1 until the difference between the generated *C* and the previous one became less than 0.05 ppm. The iteration procedure used here (i.e. the Newton–Raphson iteration method) was consistent with that used by most TBMs (Dai *et al*., 2003; Sellers *et al*., 1996).

Table 1 Input parameters of the g_m finite photosynthesis-transpiration coupled model. Fixed values were referred to Harley and Tenhunen (1991), Xue *et al*. (2017), Knauer *et al*. (2019), and Kumarathunge *et al*. (2019). The Rubisco kinetic parameters (K_c, K_o, and Γ^*) were modeled by the Arrhenius function, i.e. [exp(c-$\Delta H_a/R/T_k$)].

Input parameters	Values	Units	Parameter estimation and expression
$V_{cmax,25}$		μmol m^{-2} s^{-1}	A_n/C_i curves, Eqn. 6
ΔH_a (V_{cmax})		J mol^{-1}	
ΔS (V_{cmax})		J K^{-1} mol^{-1}	

ΔH_d (V_{cmax})	200000	J mol^{-1}	Fixed value
$J_{max,25}$		μmol m^{-2} s^{-1}	A_n/C_i curves, Eqn. 6
ΔH_a (J_{max})		J mol^{-1}	
ΔS (J_{max})		J K^{-1} mol^{-1}	
ΔH_d (J_{max})	200000	J mol^{-1}	Fixed value
$g_{m,25}$		mmol m^{-2} s^{-1}	A_n/C_i curves and chlorophyll fluorescence, anatomical traits, Eqn. 6
ΔH_a (g_m)		J mol^{-1}	
ΔS (g_m)		J K^{-1} mol^{-1}	
ΔH_d (g_m)	200000	J mol^{-1}	Fixed value
g_{fac}		unitless	Diurnal gas exchange, Eqn. 7
g_{min}		mmol m^{-2} s^{-1}	
g_{max}	900	mmol m^{-2} s^{-1}	Fixed value
O_2	210	mmol mol^{-1}	Fixed value
α	0.24	unitless	Fixed value
Θ	0.85	unitless	Fixed value
$R_{d,25}$		μmol m^{-2} s^{-1}	Gas exchange measurement
ΔH_a (R_d)		J mol^{-1}	Xue *et al.* (2017)
ΔH_a (K_o)	23720	J mol^{-1}	
c (K_o)	14.68	mmol mol^{-1}	
ΔH_a (K_c)	80990	J mol^{-1}	Bernacchi *et al.* (2002)
c (K_c)	38.28	μmol mol^{-1}	
ΔH_a (Γ*)	24460	J mol^{-1}	
c (Γ*)	13.49	μmol mol^{-1}	

(1) The g_m infinite model and parameterization

In the g_m infinite model, the CO_2 diffusion conductance from intercellular airspace to the chloroplast stroma was assumed to be infinitely large, a common practice in line with almost all TBMs. Photosynthesis is considered to be limited either by stomatal aperture/closure or by CO_2 fixation, which depends on the functioning of leaf photochemistry and/or photosynthetic enzymes. C is the intercellular CO_2 concentration. According to the Fick's first law, C can be expressed as:

$$C = C_s - 1.56A_n/g_{sw} \quad \text{(Eqn 8)}$$

V_a was estimated using the linear phase of the A_n/C_i curve (C_i from 50 to 200 ppm) and J_a was estimated using the saturated phase (C_i > 400 ppm) by referring to the studies by Xu and Badocchi (2003) and Kumarathunge *et al*. (2019). Other input parameters for the g_m infinite model were clarified in Methods S1.

(2) The g_m finite model and parameterization

In the g_m finite model, the total conductance of CO_2 diffusion from the leaf

surface to the chloroplast stroma consists of g_{sw} and g_m. Photosynthesis is limited by three major factors: stomatal conductance, mesophyll conductance, and biochemical/photochemical limitations. C is the CO_2 concentration inside the chloroplasts that depends on A_n, g_{sw}, g_m, and C_s. It can be expressed according to the Fick's first law as follows:

$$C = C_s - A_n(1.56/g_{sw} + 1.0/g_m) \quad \text{(Eqn 9)}$$

V_{cmax} and J_{max} are the maximum carboxylation rate and the maximum electron transport rate based on the CO_2 concentration in the chloroplasts, respectively. In this study, V_{cmax}, J_{max}, and g_m values were estimated using four different parameter estimation methods. The Bayesian retrieval algorithm (Zhu *et al*., 2011; Han *et al*., 2020) and the Sharkey online calculator (Sharkey *et al*., 2007) were used to estimate V_{cmax}, J_{max}, and g_m values by using the A_n/C_i curve only (abbreviated as V_{cmax_B}, J_{max_B}, g_{m_B} and V_{cmax_S}, J_{max_S}, and g_{m_S}, respectively). The chlorophyll fluorescence–gas exchange method was used to estimates g_m by using the variable J method (abbreviated as g_{m_F}), according to methods used by previous studies (Harley *et al*., 1992; Niinemets *et al*., 2009; Xue *et al*., 2016; 2017; Carriquí *et al*., 2020; 2021). The anatomy method for g_m estimation is constrained to a narrow range of leaf temperature around 25°C ($g_{m_A,25}$) (Tosens *et al*., 2012; Tomas *et al*., 2013). In this study, the prior range of parameters for the Bayesian retrieval algorithm adopted the range recommended by Zhu *et al*. (2011) and Han *et al*. (2020). The prior ranges of R_d for woody plants and herb plants were 0.01–2.0 μmol m^{-2} s^{-1} and 0.01–5.0 μmol m^{-2} s^{-1}, respectively. Notably, the unit of g_m estimated using the Sharkey online calculator and the Bayesian retrieval algorithm was μmol m^{-2} s^{-1} Pa^{-1}; therefore, it was required to be converted into mol m^{-2} s^{-1} by using the formula: $[(g_m(\text{mol m}^{-2}\,\text{s}^{-1}) = g_m(\mu\text{mol m}^{-2}\,\text{s}^{-1}\,\text{Pa}^{-1}) \times P/10]$, where P is the actual atmospheric pressure (Pa). The explicit clarity on the parameter values assumed for each parameter estimation method was referred to the Methods S1.

V_{cmax}, J_{max}, and g_m estimated using the Sharkey online calculator, Bayesian retrieval algorithm, chlorophyll fluorescence–gas exchange method, and anatomy

method were grouped to develop eight parameterization solutions to drive the g_m finite and infinite models (Table 2). For the plant species without $g_{m_A,25}$ data, model parameterization solutions adopted g_{m_B}, g_{m_S}, and g_{m_F}. g_{m_FA} at a leaf temperature of 25°C was the mean of $g_{m_F,25}$ and $g_{m_A,25}$. g_{m_FA} values at other temperatures were approximated by g_{m_F} only.

Variation in the Rubisco kinetic parameters measured *in vitro* was less than 10% amongst C_3 plant species (von Caemmerer, 2020); thus these parameters may be assumed to be identical for all vegetation types. In this study, the use of the Rubisco kinetic parameters (K_c, K_o, and Γ^*) for the g_m finite model was consistent with Bernacchi *et al*. (2002) (Table 1). However, Knauer *et al*. (2019; 2020) used two types of Rubisco kinetic parameters for model comparisons, of which one type was adopted from the study by Bernacchi *et al*. (2002) for the g_m finite model and the other type was adopted from a study by Bernacchi *et al*. (2001) for the g_m infinite model. Similarly, the Rubisco kinetic parameters in study of Bernacchi *et al*. (2001) were used for parameterization of the g_m infinite model in 141 C_3 species by Kumarathunge *et al*. (2019). The hypotheses proposed by Knauer *et al*. (2019; 2020) and Kumarathunge *et al*. (2019) were evaluated in this study. Hence, it is necessary here to parameterize the g_m infinite model by using the 2001 version in association with the Rubisco kinetic parameters.

Table 2 Eight parameterization solutions considered to drive the g_m infinite and finite photosynthesis–transpiration coupled models. V_a: the apparent maximum carboxylation rate; J_a: the apparent maximum electron transport rate; V_{cmax_B}: V_{cmax} estimated using the Bayesian retrieval algorithm; V_{cmax_S}: V_{cmax} estimated using the Sharkey online calculator; V_{cmax_SB}: the mean of V_{cmax_B} and V_{cmax_S}; J_{max_B}: J_{max} estimated using the Bayesian retrieval algorithm; J_{max_S}: J_{max} estimated using the Sharkey online calculator; J_{max_SB}: the mean of J_{max_B} and J_{max_S}; g_{m_B}: g_m estimated using the Bayesian retrieval algorithm; g_{m_S}: g_m estimated using the Sharkey online calculator; g_{m_F}: g_m estimated using the chlorophyll fluorescence–gas exchange method; $g_{m_A,25}$: g_m estimated using the anatomy method; g_{m_SBFA}: the mean of g_{m_S}, g_{m_B}, g_{m_F} and $g_{m_A,25}$; and g_{m_FA}: the mean of g_{m_F} and $g_{m_A,25}$.

Solution No.	Solution abbreviation	Configuration of each parameterization solution	Model type
1	S_S	$V_{cmax_S} + J_{max_S} + g_{m_S}$	The g_m finite model
2	S_SBFA	$V_{cmax_S} + J_{max_S} + g_{m_SBFA}$	
3	S_FA	$V_{cmax_S} + J_{max_S} + g_{m_FA}$	
4	B_B	$V_{cmax_B} + J_{max_B} + g_{m_B}$	
5	B_SBFA	$V_{cmax_B} + J_{max_B} + g_{m_SBFA}$	

6	B_FA	V_{cmax_B} + J_{max_B} + g_{m_FA}	
7	SB_FA	V_{cmax_SB} + J_{max_SB} + g_{m_FA}	
8	Inf	V_a + J_a	The g_m infinite model

Data collection for model validation

V_{cmax}, J_{max}, and g_m estimations by the four parameter estimation methods were performed using field measurements of the A_n/C_i curve plus chlorophyll fluorescence at leaf temperatures ranging from 10-15℃ to 40℃ in 19 species under 31 experimental treatments (four tropical deciduous tree species, four deciduous broadleaf tree species, seven evergreen broadleaf tree species, three C_3 crops species, and one C_3 herb and grass species) (Methods S2 and S3). Diurnal gas exchange rates were measured in 15 species under 25 treatments (Methods S2 and S3). Leaves were sampled *in-situ* immediately after the gas exchange measurement to determine the leaf anatomical structure (Methods S4). For parameter correlation analysis, the A_n/C_i curve and chlorophyll fluorescence data at 25ºC in seven gymnosperms specie, five ferns species and four herbs species were collected from literature (Carriquí *et al*., 2020; Nadal *et al*., 2018) (Methods S5). For the T_{optA}–T_{opt_gm} correlation analysis, data on T_{optA} and optimum temperature of g_m (T_{opt_gm}) estimated using the carbon isotope discrimination method ($g_{m_^{13}C}$) and the chlorophyll fluorescence–gas exchange method in five C_3 crops species, two C_3 herbs and grasses species, and one deciduous broadleaf tree species were collected from literature (Evans and von Caemmerer, 2013; Li *et al.*, 2020; Scafaro *et al.*, 2011; von Caemmerer and Evans, 2015; Warren and Dreyer, 2006; Xue *et al*., 2016) (Methods S6). Abbreviations of sampled species under different experimental treatments were referred to Methods S2–S6.

Evaluations of the g_m infinite and finite models

Independent field data, including the A_{max}–T_{leaf} curve, T_{optA}, and diurnal gas exchange, were used to validate the g_m infinite and finite models. We fitted the A_{max}–T_{leaf} curve in Eqn. 10 to obtain T_{optA} (Sall and Pettersson, 1994; Battaglia *et al*., 1996; Gunderson *et al*., 2009; Kumarathunge *et al*., 2019),

$$A_{max} = A_{opt} - b\left(T_{leaf} - T_{optA}\right) \quad \text{(Eqn 10)}$$

where A_{opt} is the A_n at T_{optA}, and parameter b (unitless) describes the curvature of A_{max} and T_{leaf}.

Root mean square error (RMSE) and Nash-Sutcliffe efficiency (NSE) coefficients were used to quantify the performance of the model (Methods S7).

Results

Temperature responses of V_{cmax}, J_{max}, and g_m

The temperature curve-fitting lines for V_{cmax_B}, V_{cmax_S}, V_{cmax_SB}, and V_a increased rapidly with increase in T_{leaf} from 10°C to 35°C, and began to decrease after reaching a peak (about 300 μmol m^{-2} s^{-1} for V_{cmax_B}, V_{cmax_S}, and V_{cmax_SB}; 180 μmol m^{-2} s^{-1} for V_a) at a leaf temperature around 35°C. V_{cmax_B}, V_{cmax_S}, and V_{cmax_SB} presented a similar behavior ($p > 0.1$, Fig. 1a and Figs. S1a-ae), except at high leaf temperatures ≥ 35°C. Despite V_{cmax_SB} was significantly higher by 43.9% in average than V_a at 25°C, considerable scatter in the difference for the two variables was observed (Table S1). There were similar values at each leaf temperature among temperature response curves of J_{max_B}, J_{max_S}, J_{max_SB}, and J_a (Fig. 1b), with the difference among them being less than 6% at 25°C and the optimal temperatures changing around 32–34°C (Figs. S2a-ae and Table S2). The g_{m_B} temperature curve-fitting line was overlapped with that of g_{m_S} (Fig. 1c), whereas both had significantly higher values by 69% and 58% than that of g_{m_FA} at 25°C, respectively (Table S3). However, the g_{m_S} temperature curve-fitting line did not well overlap with the 95% confidence interval because of irregular observations in g_{m_S} temperature response among sampled species/treatments (Figs. S3a-ae). The temperature curve-fitting lines for g_{m_B}, g_{m_S}, and g_{m_FA} exhibited larger variations in T_{opt_gm}, ranging from 27 to 32°C, which were lower by 15.7% and 10.6% in average as compared to optimal temperatures for V_{cmax} (i.e. V_{cmax_B}, V_{cmax_S}, and V_{cmax_SB}) and J_{max} (i.e. J_{max_B}, J_{max_S}, J_{max_SB}), respectively.

The boxplot minimum value of ΔH_a was 49.2 KJ mol^{-1} for V_{cmax_B}, 52.3 KJ mol^{-1} for V_{cmax_S}, 37.6 KJ mol^{-1} for V_{cmax_SB}, and 65.6 KJ mol^{-1} for V_a (Fig. 1d). For J_{max_B},

J_{max_S}, J_{max_SB}, and J_a, their minimum values were 22.2, 20.8, 22.6, and 23.6 KJ mol^{-1}, respectively (Fig. 1e). Similarities in the minimum value that was close to zero were observed for g_{m_B}, g_{m_S}, and g_{m_FA} (Fig. 1f). Zero value in ΔH_a was found in Pop_WC for g_{m_B}, in Pop_CW for g_{m_S}, and in E_sal and E_mdel for g_{m_FA} (Table S3 and Figs. S3u, t, q, and r). There were similarities in the interquartile range (IQR) of ΔH_a among V_{cmax_B}, V_{cmax_S}, V_{cmax_SB}, and V_a, so did the ΔH_a of the four J_{max} types and the ΔH_a of the three g_m types. However, larger ranges in the IQR of ΔH_a for g_m (i.e. g_{m_B}, g_{m_S}, and g_{m_FA}) than those of J_{max} and V_{cmax} were clearly observed and coefficient of variation (*CV*) in ΔH_a of g_m (i.e. g_{m_B}, g_{m_S}, and g_{m_FA}) was amplified in average by 135.2% (Table S3). The IQR of ΔS for V_{cmax_B}, V_{cmax_S}, V_{cmax_SB}, and V_a was 5.1, 20.2, 8.3, and 15.6 J K^{-1} mol^{-1}, respectively (Fig. 1g). Similarities in the IQR of ΔS among J_{max_B}, J_{max_S}, J_{max_SB}, and J_a temperature responses were evident (Fig. 1h and Table S2). Whereas, the first quartile (Q1) values of ΔS for g_m (i.e. g_{m_B}, g_{m_S}, and g_{m_FA}) were similar or slightly higher than the third quartile (Q3) values of V_{cmax} (i.e. V_{cmax_B}, V_{cmax_S}, and V_{cmax_SB}) and J_{max} (i.e. J_{max_B}, J_{max_S}, and J_{max_SB}) (i.e. mean of the Q1 value for g_m was 644.5 J K^{-1} mol^{-1}; mean of the Q3 value for V_{cmax} was 644.1 J K^{-1} mol^{-1}, and mean of the Q3 value for J_{max} was 647.5 J K^{-1} mol^{-1}). The mean value of ΔS across g_{m_B}, g_{m_S}, and g_{m_FA} temperature curves was 654 J K^{-1} mol^{-1}, whereas it was 639 J K^{-1} mol^{-1} for J_{max} (i.e. J_{max_B}, J_{max_S}, and J_{max_SB}) and 637 J K^{-1} mol^{-1} for V_{cmax} (i.e. V_{cmax_B}, V_{cmax_S}, and V_{cmax_SB}) (Table S1-S3). The *CV*s of ΔS for g_{m_B}, g_{m_S}, and g_{m_FA} temperature curves were 1.74%, 2.88%, and 2.2%, respectively, while the corresponding *CV*s of ΔH_a were 58.45%, 78.98%, and 53.26%, respectively (Table S3). These results suggested: greater variations in ΔH_a and ΔS of g_m than those of V_{cmax} and J_{max}; large variations in ΔH_a and relatively small variations in ΔS for g_m; and greater values in ΔS for g_m than those for V_{cmax} and J_{max}.

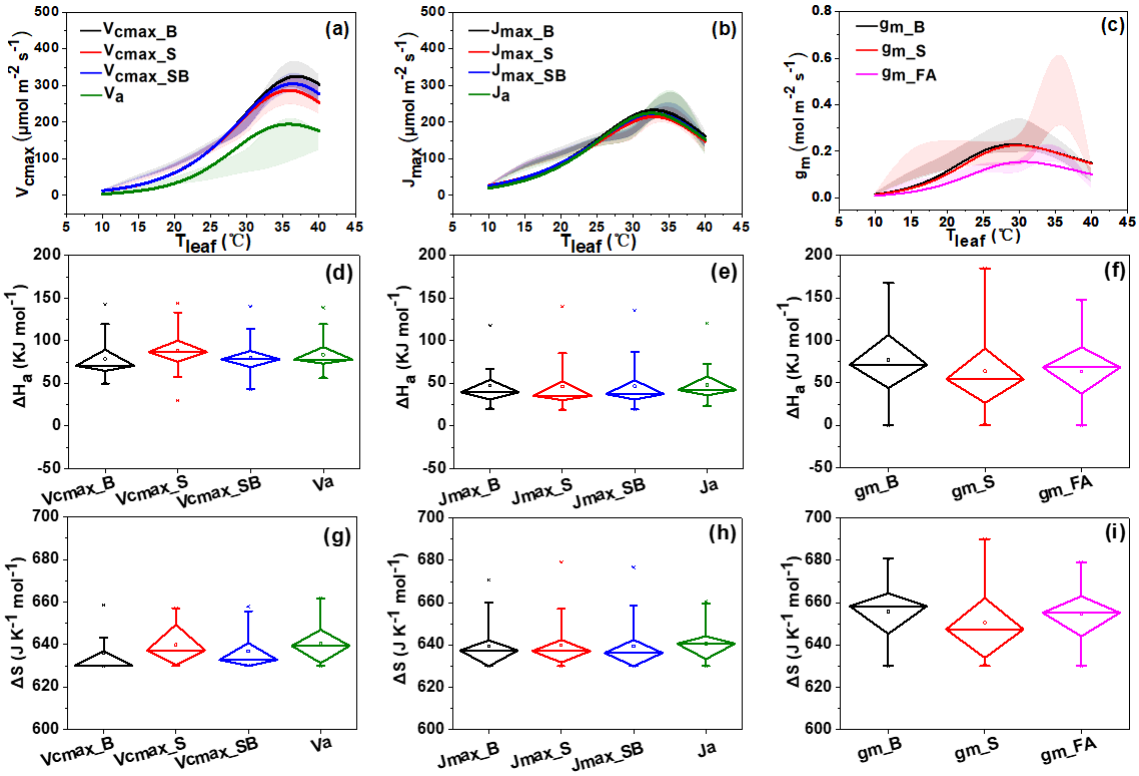

Fig. 1 V_a and V_{cmax}, J_a and J_{max}, and g_m temperature response curves performed by fitting the mean of parameter estimations of 19 species at 31 treatments using the Eqn. 6 and were labeled by shadow zones (Figs. 1a-c). The shadow zone for each curve-fitting line was the 95% confidence interval of parameter estimations of all sampled species/treatments. Distribution features of ΔH_a and ΔS values that determine V_a and V_{cmax}, J_a and J_{max}, and g_m temperature response curves in all sampled species/treatments were displayed using the box-plot (Figs. 1d-i). The curve-fitting lines of V_a and V_{cmax}, J_a and J_{max}, and g_m temperature response for individual species/treatment were shown in Supporting Information Figs. S1-S3. V_{cmax}, J_{max}, and g_m values were estimated using different parameter estimation methods, namely the Bayesian retrieval algorithm (V_{cmax_B}, J_{max_B}, and g_{m_B}, black solid line), the Sharkey online electronic calculator (V_{cmax_S}, J_{max_S}, and g_{m_S}, red solid line), the mean of V_{cmax_B} and V_{cmax_S} and the mean of J_{max_B}, and J_{max_S} (V_{cmax_SB} and J_{max_SB}, blue solid line), the mean of g_m estimated using the chlorophyll fluorescence–gas exchange and anatomy methods (g_{m_FA}, pink solid line), and the apparent maximum carboxylation rate and the apparent maximum electron transport rate (V_a and J_a, green solid line).

Comparisons between gas exchange observations and simulations by the g_m finite and infinite models

For the A_{max}–T_{leaf} curves measured at ambient C_a = 400–450 ppm, the slopes of the linear regression between observations and simulations by the S_S, S_SBFA, and S_FA parameterization schemes were 0.87, 0.91, and 1.00, respectively (Figs. 2a-c). The adjusted R^2 (adj.R^2) values for the three schemes were 0.81, 0.86, and 0.90, respectively, and the corresponding NSE values were 0.79, 0.84, and 0.88. The RMSE values of the three parameterization schemes accounted for 24%, 22%, and 19% of the mean A_{max} ($A_{max,mean}$ = 12.47 μmol m^{-2} s^{-1}). The predicted A_{max} values from the

S_S and S_SBFA schemes were 11% and 7% higher than the $A_{max,mean}$, respectively (Figs. S4a-ae). These results suggested that g_m estimation using the chlorophyll fluorescence–gas exchange method and anatomy method was more reasonable. In line with the results obtained from S_S, S_SBFA, and S_FA schemes, the B_FA scheme fitted A_{max} at each temperature better than the B_B and B_SBFA schemes (Figs. 2d-f and Figs. S4a-ae), which further suggested that the configuration of g_{m_FA} for g_m estimation was more reasonable. As shown in Figs. 1a and b, the values of V_{cmax_B} and V_{cmax_S} and those of J_{max_B} and J_{max_S} at each temperature were similar to each other. Therefore, we considered the possible effects of the combination of V_{cmax} or J_{max} estimations using the Bayesian retrieval algorithm and Sharkey online calculator on A_{max} simulations (the SB_FA scheme in Figs. S4a-ae). The NSE value for the SB_FA scheme (0.92) was 5% and 1% higher, whereas the ratio of RMSE to $A_{max,mean}$ was 21% and 12% lower than those for the S_FA and B_FA schemes suggesting better A_{max} predictions using the parameter configuration scheme by considering V_{cmax_SB}, J_{max_SB}, and g_{m_FA}. The adj.R^2, NSE, and the ratio of RMSE to $A_{max,mean}$ were 0.85, 0.73, and 28%, respectively (Fig. 2h), indicating that although the g_m infinite model is generally credible in estimating the A_{max}–T_{leaf} curve, the prediction errors in this model are relatively larger. We found that A_{max} predictions using the g_m infinite model were significantly higher (16%) than the observations (partially for 30–40°C, Figs. S4a-ae). Additionally, numerical simulation indicated that the g_m finite model driven by the g_m temperature function without considering the deactivation stage significantly overestimated A_{max} at higher temperatures 30–35–40°C by 10.99%, 32.51%, 64.06%, respectively. The results obtained from the eight parameterization schemes at C_a = 600–630 ppm were similar to those at C_a = 400–450 ppm (Figs. 2a-h and Figs. S5a-ae). These results indicated that the g_m finite model driven by the SB_FA scheme could predict A_{max} more accurately than the g_m infinite model.

Figs. 2i-l shows the comparisons in diurnal A_n, E, and g_{sw} between observations and predictions using the g_m infinite model and the g_m finite model that is forced by the parameterization scheme SB_FA (detailed comparisons in each species/treatment

shown in Figs. S6-S8). The adj.R^2 values for A_n, E, and g_{sw} predicted using the g_m finite model were 0.88, 0.85, and 0.78, respectively, whereas those predicted using the g_m infinite model were 0.87, 0.83, and 0.76, respectively. The NSE values for the three variables for the g_m finite model were 0.88, 0.85, and 0.76, respectively, and those for the g_m infinite model were 0.76, 0.75, and 0.74, respectively. The ratio of RMSE to the mean of A_n, E, and g_{sw} for the g_m finite model was 27%, 34%, and 40%, respectively, whereas that for the g_m infinite model was 38%, 45%, and 42%, respectively. Meanwhile, significant overestimations in simulated A_n under heat shocking conditions (i.e. T_{leaf} from > 30°C) by 25%–40% by using the g_m infinite model were observed (Fig. 2l and Fig. S9). These results suggested that the g_m finite model is superior to the g_m infinite model in predicting diurnal gas exchange under a wide range of growth conditions.

For the diurnal changes in A_n, the adj.R^2 and NSE for the g_m finite model were improved by 1% and 12% compared with those for the g_m infinite model. For the diurnal changes in E, the adj.R^2 and NSE for the g_m finite model improved by 2% and 10% compared with those for the g_m infinite model. These results suggested that the effects of g_m finite expression on photosynthesis and transpiration estimations were almost equally stronger.

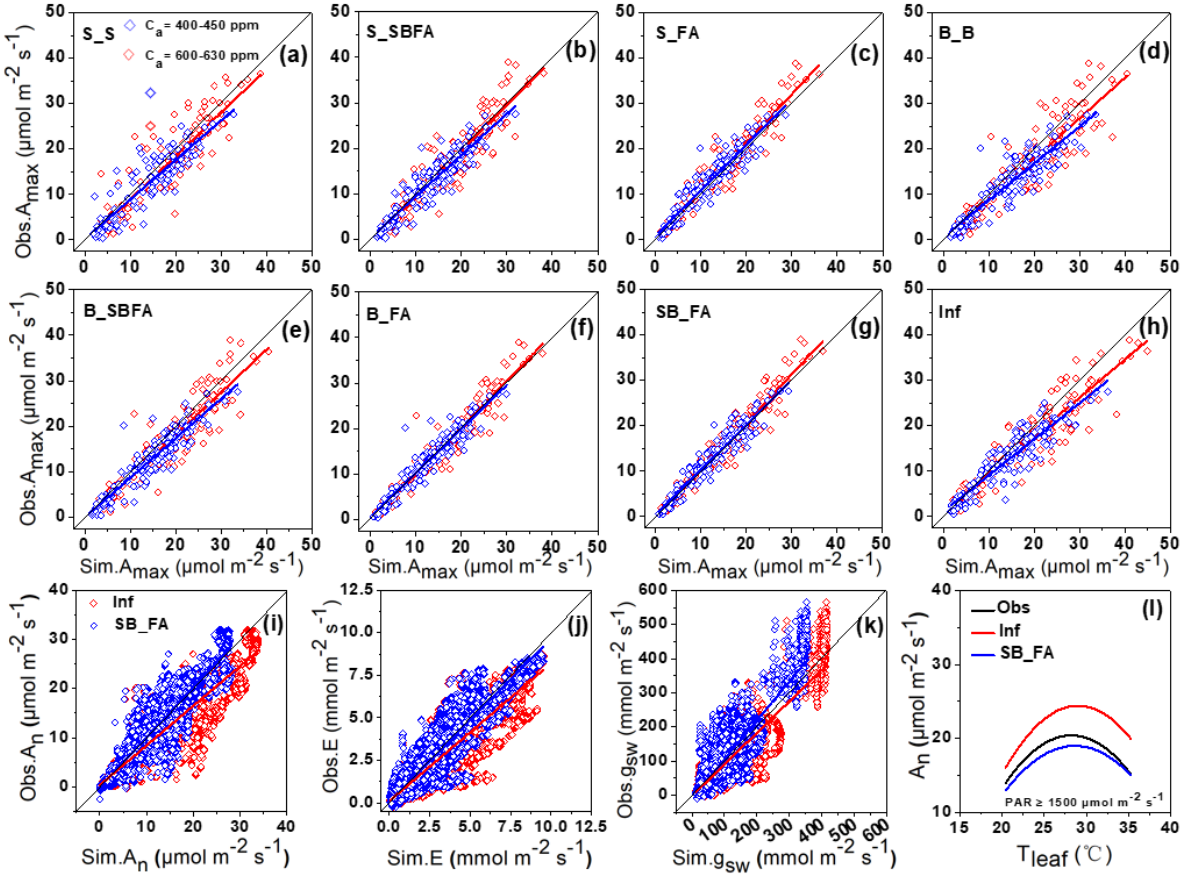

Fig. 2 Scatter plots showing comparisons in A_{max} observations and predictions between the g_m infinite and finite models that are forced by eight parameterization schemes (Figs. 2a-h, S_S, S_SBFA, S_FA, B_B, B_SBFA, B_FA, SB_FA, and Inf). The blue solid line signifies the linear regression fit between observations at C_a = 400-450 ppm and predictions, and the red solid line signifies the linear regression fit between observations at C_a = 600-630 ppm and predictions. Scatter diagrams in Figs. 2i-k showing comparisons in the diurnal assimilation rate (A_n), transpiration rate (E), and stomatal conductance (g_{sw}) between observations and predictions using the g_m infinite model (red diamonds) and the g_m finite model that is forced by the parameterization scheme SB_FA (blue diamonds). The black solid line represents the 1:1 line. Curve-fitting lines in Fig. 2l show comparisons in diurnal A_n at *PAR* greater than 1500 μmol m^{-2} s^{-1} and across a wide range of leaf temperatures between observations (black line) and predictions using the g_m infinite model (red line) and the g_m finite model that is forced by the parameterization scheme SB_FA (blue line). C_a: CO_2 concentration at leaf surface; *PAR*: photosynthetically active radiation.

Statistical correlations between T_{optA} and photosynthetic parameters

The linear regression slope and adj.R^2 values between T_{optA} predictions using the g_m finite model and observations were 0.67 and 0.85, respectively, whereas those obtained using the g_m infinite model were 0.88 and 0.18, respectively (Fig. 3a). T_{optA} predicted using the g_m finite model displayed a better correlation with the observations. We observed that T_{optA} observations had a significant positive correlation with the T_{opt_gm} derived from g_{m_FA} and $g_{m_^{13}C}$ temperature responses, and

the adj.R^2 value reached 0.58 (Fig. 3b). No significant correlations were found among T_{optA}–ΔH_a of g_{m_FA}, T_{optA}–$g_{m_FA,25}$, and T_{optA}–$J_{max_SB,25}/V_{cmax_SB,25}$ (Fig. S10).

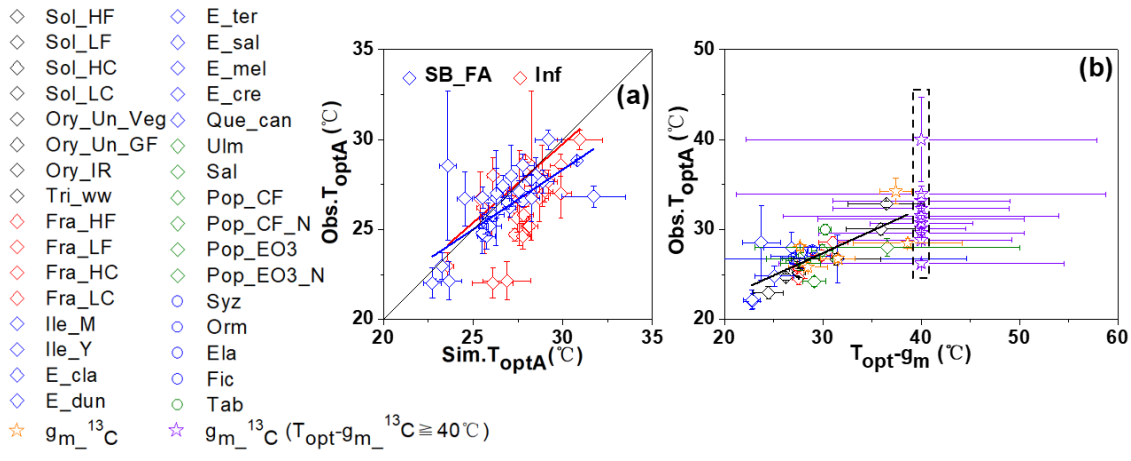

Fig. 3 Scatter diagrams showing comparisons in photosynthesis optimal temperature (T_{optA}) between observations (Obs.T_{optA}) and predictions using the g_m finite model forced by the parameterization solution SB_FA (Sim.T_{optA}, blue circles) and by the g_m infinite model (red circles) (a) and the statistical correlation for Obs.T_{optA} and g_m optimal temperature ($T_{opt\text{-}g_m}$) across different plant functional types (b). The black solid line in Fig. 3a represents the 1:1 line. The red and blue lines in Fig. 3a and the black line in Fig. 3b are the linear regression fit. $T_{opt\text{-}g_m}$ in g_m temperature response estimated using the ^{13}C discrimination method greater than and equal to 40°C ($T_{opt\text{-}g_m_^{13}C}$ values ≥ 40°C were unified to be 40°C indicated by purple stars inside the dashed square) was not included for statistical correlation analysis in Fig. 3b. The sampled species/treatments are classified into six plant functional types (PFTs): black diamonds for C_3 crops (C_3C), blue diamonds for evergreen broadleaf trees (EBF), green diamonds for deciduous broadleaf trees (DBF), red diamonds for C_3 herbs and grasses (C_3G), blue circles for tropical evergreen broadleaf trees (TRF), and green circles for tropical deciduous broadleaf trees (TDF).

Statistical correlations among photosynthetic parameters estimated by four parameter estimation methods

$g_{m_F,25}$ was positively correlated with $g_{m_A,25}$, whereas the adj.R^2 was 0.22, and the linear regression slope was 0.57, which is much lower than 1.0 (Fig. 4a), primarily because of large discrepancies between the two variables in rice plants. The two variables strongly correlated in other sampled species/treatments with the adj.R^2 of 0.76 and the slope of 0.80. A significant exponential correlation was found between $g_{m_FA,25}$ and $g_{m_SB,25}$ (adj.R^2 = 0.67, $p < 0.01$, Fig. 4b), so did the correlation between $g_{m_F,40}$ and $g_{m_SB,40}$ (gray circles in Fig. 4b), with a close agreement found at low g_m < 0.15 mol m^{-2} s^{-1}. A negative correlation for $g_{m_FA,25}$ and the difference between $V_{cmax_SB,25}$ and $V_{a,25}$ was found (adj.R^2 = 0.47, $p < 0.05$, Fig. 4c). $J_{max_SB,25}$ was closely related to $V_{cmax_SB,25}$ (adj.R^2 = 0.83, $p < 0.01$, Fig. 4d).

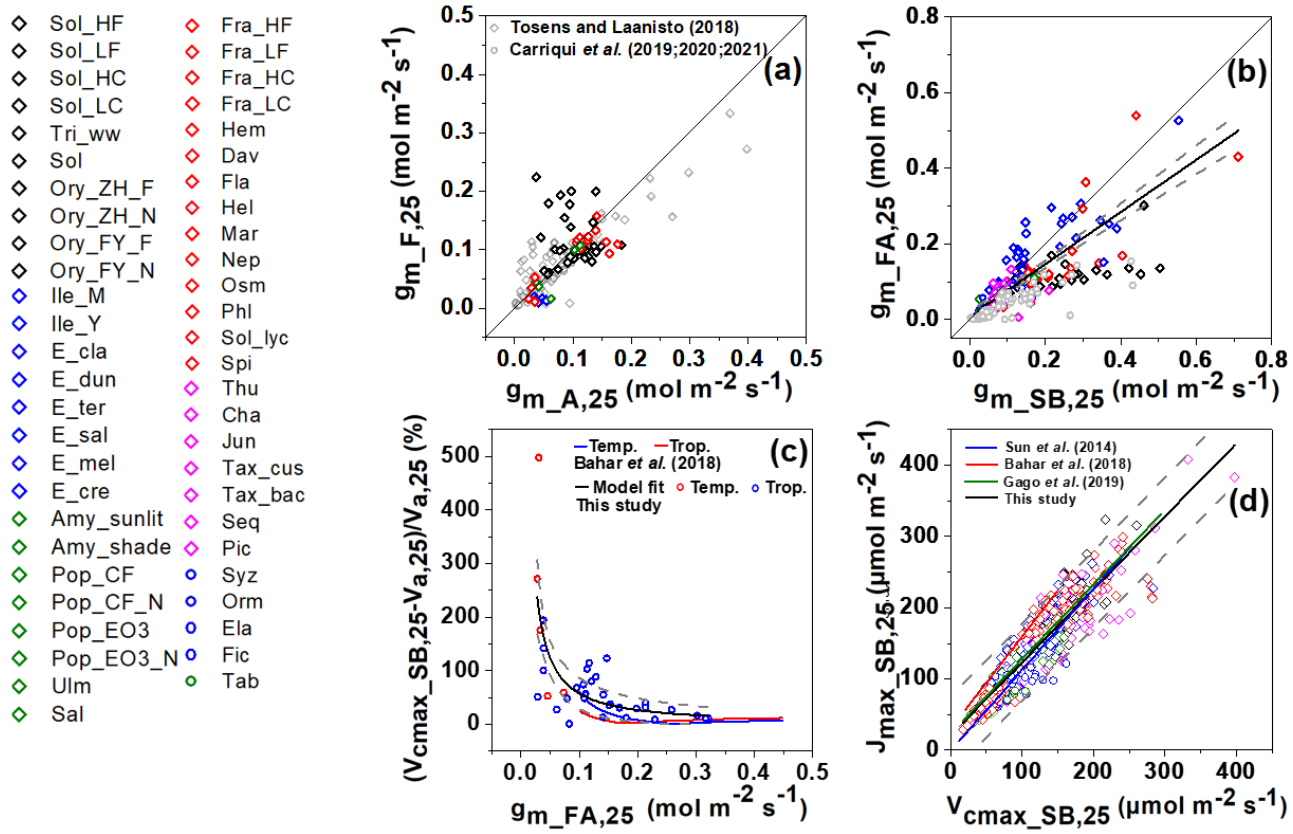

Fig. 4 Statistical correlations for $g_{m_F,25}$–$g_{m_A,25}$ (a), for $g_{m_FA,25}$–$g_{m_SB,25}$ (b), for $g_{m_FA,25}$–the difference between $V_{cmax_SB,25}$ and $V_{a,25}$ (c), and for $J_{max_SB,25}$–$V_{cmax_SB,25}$ (d) in sampled species/treatments. The sampled species/treatments in Figs. 4a, b and d are classified into six plant functional types (PFTs): black diamonds for C_3 crops (C_3C), blue diamonds for evergreen broadleaf trees (EBF), green diamonds for deciduous broadleaf trees (DBF), red diamonds for C_3 herbs and grasses (C_3G), blue circles for tropical evergreen broadleaf trees (TRF), and green circles for tropical deciduous broadleaf trees (TDF). The paired datasets for $g_{m_F,25}$ and $g_{m_A,25}$ in studies of Tosens and Laanisto (2018) and Carriquí *et al*. (2019; 2020; 2021) were added in Fig. 4a (grey diamonds and circles). $g_{m_SB,25}$ greater than 1.5 mol m^{-2} s^{-1} are regarded as outliers and are not shown. Gly_amb, Pop_WC, and Pop_CW are not shown as they do not have the observation data at a leaf temperature of 25°C. $g_{m_F,40}$ and $g_{m_SB,40}$ datasets were added (gray circles) in Fig. 4b for comparison with the $g_{m_FA,25}$–$g_{m_SB,25}$ correlation. V_{cmax_Cc} and V_{cmax_Ci} values in temperate species (Temp.: *Phyllocladus aspleniifolius*) and tropical species (Trop.: *Litsea leefeana*) in the study of Bahar *et al*. (2018) were used to calculate the difference of the two variables as shown in Fig. 4c (blue and red lines, respectively). V_{cmax_Cc} in their study (i.e. $V_{cmax,25}$) was derived from the A_n/C_c curve that is converted from the A_n/C_i curve by assuming a constant g_m at the entire C_i range. V_{cmax_Ci} is the apparent V_{cmax} (i.e. $V_{a,25}$) derived from the A_n/C_i curve in their study, which is equivalent to V_a in our study. The $g_{m,25}$ in their study was estimated using the ^{13}C isotope discrimination method. The dashed lines in grey color represent the 95% prediction intervals of the nonlinear regression. Temp.: temperate species; Trop.: tropical species.

Discussion

Superiority of the g_m finite model and an optimized parameterization solution that excludes the equifinality phenomenon

The A_{max}–T_{leaf} curves were accurately predicted using the g_m infinite model only

in 15 species/treatments (Figs. S4d, j-s, y, aa, ad, and ae), whereas A_{max} values at higher temperatures (30–40°C) were largely overestimated in other sampled species/treatments. Poor modeling accuracies were also evident in the simulation of diurnal gas exchange rates (Fig. 2l and Figs. S6c, e, h, k, l, n, p, and q). It aligned with the previous reports in rice and winter wheat by Xue *et al*. (2016) and in *Quercus ilex* by Niinemets *et al*. (2009) who found that the photosynthesis model that does not explicitly consider g_m cannot always predict leaf gas exchange accurately. The g_m finite model considers the dependent effects of chloroplast CO_2 concentration on the assimilation rate, stomatal and mesophyll resistance, and leaf surface CO_2 concentration (von Caemmerer, 2013; 2020). The relationships among CO_2 diffusion flux, CO_2 concentration gradient between the leaf surface and chloroplasts, and gas diffusion resistance may be approximated using the Fick's first law (Harley *et al*., 1992; Xue *et al*., 2017), as shown in Eqn. 9. Simulation results in gas exchange in 19 species under a wide range of growth conditions proved that the g_m finite model has good transferability and high prediction capacity, due to which the model can be applied to as many C_3 species as possible. The g_m finite model developed in this study can be conveniently substituted into most TBMs by simply replacing ($C_i = C_s - 1.56A_n/g_{sw}$) as given in Eqn. 9.

V_{cmax}, J_{max}, and g_m temperature responses are key photosynthetic parameters of the g_m finite model. Despite a "one-point" method has been proposed to quantify V_{cmax}, there is no consensus that this method can be widely used (Burnett *et al*. 2019). One way to determine V_{cmax} is from the A_n/C_c curve that is converted from the A_n/C_i curve using a value for g_m determined at ambient CO_2 and assuming a constant g_m for the entire range of C_i (Manter and Kerrigan, 2004; Bahar *et al*., 2018). Whereas, the conversion of A_n/C_i to A_n/C_c may not be true at low g_m values under certain conditions (Flexas *et al*., 2007). The key photosynthetic parameters can also be quantified using the curve-fitting methods applied to the A_n/C_i curve; for example, the Bayesian retrieval algorithm and the Sharkey online calculator (Sharkey *et al*., 2007; von Caemmerer*et al*., 2009; Gu *et al*., 2010; Zhu *et al*., 2011; von Caemmerer, 2013). The

curve-fitting methods that simultaneously quantify the three key photosynthetic parameters may have the equifinality phenomenon (i.e., similar simulation results can be achieved with different initial conditions), because of a curvilinear negative correlation between V_{cmax} estimation and g_m (von Caemmerer, 2013) that changes steeply at the lower range of g_m (generally < 0.1 mol m^{-2} s^{-1}) (Bahar *et al*., 2018). For the parameterization of the g_m finite model, V_{cmax}, J_{max}, and g_m values were simultaneously estimated by the Bayesian retrieval algorithm, so did the Sharkey online calculator. Importantly, g_m was also determined using the chlorophyll fluorescence–gas exchange method and the anatomy method. Our results indicated that the g_{m_B} temperature responses were significantly different from the g_{m_S} temperature responses in terms of absolute values at 25ºC and ΔH_a in most sampled species/treatments (Figs. S3a-b, d, f-i, l, o-t, y, aa-ac), whereas similarities in the temperature response for either V_{cmax} or J_{max} were found between the two curve-fitting methods. It implied that the differences in V_{cmax} observed at high temperatures between the two methods (Fig. 1a) were likely not related to g_m estimation. A close agreement between the $g_{m_F,25}$ and $g_{m_A,25}$ (Fig. 4a) and between $g_{m_FA,25/40}$ and $g_{m_SB,25/40}$, especially at the lower range < 0.15 mol m^{-2} s^{-1} (Fig. 4b), was evident, respectively. Furthermore, there is a close agreement in $T_{opt_}g_m$ between the chlorophyll fluorescence–gas exchange method and the Bayesian retrieval method (adj.R^2 = 0.58 and the regression slope = 0.81, Fig. S3a-ae). Results suggested that the four parameter estimation methods give similar g_m estimations, especially at the lower range. The consequence of variations in g_m on estimation of V_{cmax} on C_c and C_i bases in this study was consistent with the reports by Bahar *et al*. (2018) (Fig. 4c). Hence, the estimations in V_{cmax} by fusing the Bayesian retrieval algorithm and the Sharkey online calculator are reasonable. Furthermore, we found a significantly linear correlation between $V_{cmax_SB,25}$ and $J_{max_SB,25}$ (Fig. 4d), which falls between the reports by Bahar *et al*. (2018) and Sun *et al*. (2014) and overlaps with the reports by Gago *et al*. (2019). These results suggested that the four parameter estimation methods are independent in the measurements taken for parameter estimation and optimization

algorithms, namely the optimized parameterization scheme (i.e. the SB_FA scheme, discussed below) is physiologically meaningful, which excludes the equifinality phenomenon.

In the present study, a close relationship between $g_{m_F,25}$ and $g_{m_A,25}$ was observed in most sampled species/treatments (Fig. 4a). The close correspondence between the two variables has been also reported in many other C_3 species (Tosens and Laanisto, 2018; Carriquí *et al*., 2019; 2020; 2021) (grey symbols shown in Fig. 4a). Mesophyll conductance is a complex three-dimensional trait that is probably determined by both biochemical and anatomical features. The chlorophyll fluorescence method compares gas exchange signal with the optical signal which may vary with the depth through the mesophyll tissue (Evans, 2021). These variations may explain minor discrepancies between $g_{m_A,25}$ and $g_{m_F,25}$ in most sampled species/treatments (Fig. 4a). Carriquí *et al*. (2020) reported that the cell wall composition is a key factor in the g_m setting in sclerophyll species. The constant values in model parameters of the anatomy g_m estimation method for vascular plants such as the ratio of cell wall porosity to tortuosity (P_{cw}) may also contribute to the discrepancies. In this study, $g_{m_F,25}$ was found to be significantly higher than $g_{m_A,25}$ in rice. An extremely dense distribution of mesophyll cells in rice was observed (ultrastructure images not shown). The total length of the chloroplast facing the intercellular space (l_c) in association with $g_{m_A,25}$ by using the ultrathin sections was probably underestimated in rice because of the exclusion of tightly adjacent parts of two mesophyll cells in the sampling fields of view.

As shown in Figs. 2a and d, g_m estimation using the A_n/C_i curve only through the Bayesian retrieval algorithm or the Sharkey online calculator can accurately predict leaf gas exchange rates in some species/treatments, whereas cannot in others. A better modeling performance was obtained by the S_FA scheme (i.e. V_{cmax_S}+J_{max_S}+g_{m_FA}) than the S_S scheme (i.e. V_{cmax_S}+J_{max_S}+g_{m_S}). Our results are similar to reports by Sharkey *et al*. (2007): if chlorophyll fluorescence data are available, it could be possible to estimate g_m from those data to ameliorate reliability of modeling

performance. Results suggested the SB_FA solution (i.e. V_{cmax_SB}+J_{max_SB}+g_{m_FA}) that can predict the photosynthesis and transpiration better than other parameterization solutions as the optimized parameterization solution for the g_m finite model.

Temperature responses characteristics of g_m

A g_m response to temperature has been reported in some species, but not in others (Scafaro *et al*., 2011; von Caemmerer and Evans, 2015; Shrestha *et al*., 2019; Evans, 2021; Li *et al*., 2020), partially due to differences in g_m estimation methods used by them, as seen in great variations in g_m temperature response obtained by different estimation methods (Fig. 1c and Figs. S3a-ae). We argued that the g_m estimated using the parameter estimation method that can accurately fit the A_{max}–T_{leaf} curve and diurnal gas exchange rates has higher credibility than those that cannot predict accurately. Results of our study suggested that 90% of the sampled species under well-watered conditions exhibit a significant response of g_m to temperature. Inter-species variations in both ΔH_a and ΔS for g_m were significantly greater than those of V_{cmax} and J_{max}. Large variations in ΔH_a signify significant changes in g_m temperature response across species, which is in agreement with the results of the studies by Shrestha *et al*. (2019), von Caemmerer and Evans (2015), and Evans (2021). The two-components modeling method developed by von Caemmerer and Evans (2015) produced ΔH_a for CO_2 permeability through the membranes, ranging between 36 and 76 kJ mol^{-1}. Using the isolated pea leaf plasma membranes, Zhao *et al*. (2017) reported ΔH_a for CO_2 permeability of 30.2 and 52.4 kJ mol^{-1} at high and low internal carbonic anhydrase (CA) concentrations. Results of our study reported the lower and upper limits of the 95% confidence interval of ΔH_a for g_{m_FA} were 50.14 and 76.12 kJ mol^{-1}, respectively. The determined ΔH_a values of our study are similar to the ranges reported by von Caemmerer and Evans (2015) and Zhao *et al*. (2017). The rates of CO_2 diffusion in the membranes and during the liquid phase reflect the amount of CO_2-permeable and transport enzyme proteins, their thermal stabilities, and the structural components of cell wall. A common or distinct set of aquaporins in the

membranes and the associating proteins such as CA inside the vesicles that affect ΔH_a for CO_2 permeability/diffusion (Zhao *et al*., 2017) likely vary greatly in expression levels and the associating heterotetramers among C_3 species (Otto *et al*., 2010; Momayyezi *et al*., 2020). Hence, the determined large variations in temperature response attributes of g_m are reasonable.

The temperatures at which V_{cmax} and J_{max} deactivate were usually higher than 35°C and even 40°C in most sampled species. They are similar to the findings in tobacco (Bernacchi*et al*., 2001), rice (Xue *et al*., 2016), and poplar (Silim *et al*., 2010; Xu *et al*., 2020). We found that g_m deactivation temperatures were lower than those for V_{cmax} and J_{max} (Figs. 1a-c), which are similar to reports by Xu *et al*. (2020) and Warren and Dreyer (2006). Meanwhile, better accuracy in leaf gas exchange predictions was obtained using the temperature peak function for g_m than the monotone increasing function. Results highlighted importance of incorporating the deactivation stage of g_m into leaf photosynthesis model for better modeling accuracy. A rapid change in fluidity of plasma membrane was observed within 1-3 min after heat shock of 37°C in *A. thaliana* and wheat (Zheng *et al*., 2012; Abdelrahman *et al*., 2020). Elevated temperature increases membrane permeability. During a 40°C, 5–15 min heat stress Triandafillou *et al*. (2020) found that *Saccharomyces cerevisiae* cells rapidly acidify from a pH of 7.5 to a range of slightly acidic pH values around 6.8 due to proton influx, which could constrain the CA stability by 20–30% (Wang *et al*., 2016). The transient intracellular acidification induced by heat stress is broadly conserved in eukaryotes. Changes in fluidity and permeability of plasma membrane at elevated temperatures (Niu and Xiang, 2018) that cause proton influx and impact the CA stability may cause the decline of g_m by 10–20% at elevated temperature from 30°C to 40°C (Fig. 1c).

Effects of the g_m finite expression on photosynthesis and transpiration

Kumarathunge *et al*. (2019) proposed that the variation in T_{optA} among species can be explained by biochemical restrictions ($J_{a,25}/V_{a,25}$). V_a and J_a are referred to as

the apparent maximum carboxylation rate and electron transport rate, respectively, and both these parameters, particularly V_a, are numerically and physiologically different from V_{cmax} and J_{max}. A similar result of an asymmetric effect of g_m estimation on V_{cmax} and J_{max} estimations was reported by Manter and Kerrigan (2004) and Sun *et al*. (2014). Hence, we may argue that V_a not only represents the Rubisco carboxylation rate but also embeds the g_m effects. Stripping off the g_m effects from $V_{a,25}$ would cause changes in $J_{a,25}/V_{a,25}$ and then cause significant changes in the T_{optA}–$J_{a,25}/V_{a,25}$ correlation. Our results suggested that T_{optA} has a significant linear correlation with T_{opt_gm} but not JVr, ΔH_a of g_{m_FA}, and $g_{m_FA,25}$, implying that T_{optA} is probably related to g_m temperature response characteristics. Whereas, the plasticity in T_{optA} was not fully related to g_m because only 58% of the variations in T_{optA} were explained by g_m. Changes in the Rubisco kinetic properties, such as thermal stability of Rubisco activase (Salvucci and Crafts-Brandner, 2004), could be an important mechanism.

Knauer *et al*. (2020) argued that the g_m finite expression has significant effects on photosynthesis estimation and that the effects of g_m on transpiration are marginal. Conversely, we found that the effects of the g_m finite expression on photosynthesis and transpiration simulations are equally stronger. Significant effects on transpiration estimation were probably achieved through better predictions of g_{sw} because transpiration is a product of *VPD* and g_{sw}. Across diverse species, g_m is strongly linked with g_{sw} and leaf hydraulic conductance through the g_m linkage to extra-xylem components (Flexas *et al*., 2013) such as the plasma membrane intrinsic proteins (PIPs) subfamily of aquaporins (Groszmann *et al*., 2017). Physiological mechanisms underlying the integrated hydraulic–photosynthetic system explained the observed effects of the g_m finite expression on photosynthesis and transpiration.

Conclusions

In this study, we developed a g_m finite photosynthesis-transpiration coupled model that can be directly applicable for most TBMs and also proposed an optimized parameterization solution. The g_m finite model driven by the parameterization theme

of V_{cmax_SB}, J_{max_SB} and g_{m_FA} could well predict A_{max}–T_{leaf} curves and diurnal gas exchange rates in all sampled species under various experimental treatments. However, the g_m infinite model cannot always accurately track variations in photosynthesis and transpiration. Results suggested large variations in ΔH_a and ΔS for g_m. T_{optA} was related to thermal attributes of g_m not JVr. Meanwhile, the explicit g_m expression had equally important effects on photosynthesis and transpiration estimations at plant species level. Results of our study proved that the g_m finite expression in most TBMs is important for better understanding effects of g_m on photosynthesis and transpiration under climate change.

Acknowledgements

This research was supported by the Fundamental Research Funds for the Central Universities (lzujbky-2020-28) and the National Natural Science Foundation of China (32001129). Sincere thanks are dedicated to Dr. John R. Evans for his comments on the manuscript. We are also grateful to Dandan Liu and Xiao Song for their helps on field data collection. The authors declare that they have no conflicts of interest.

Author contributions

WX: design of the research and funding, data analysis, collection and interpretation, and manuscript writing and revision. HL: data analysis, collection and interpretation, and manuscript writing. JE, MC, MN, TH, and CW: data collection and analysis, manuscript revision. J-F H, J-L Z, Z-G Y and X-W F: data collection and part work of data analysis.

Data availability

The data that support the findings of this study are available from the corresponding author upon reasonable request. MATLAB script for Bayesian retrieval algorithm and the g_m finite photosynthesis-transpiration coupled model compiled by FORTRAN can be obtained through directly contacting the correspondence author.

References

Abdelrahman M, Ishii T, El-Sayed M, Phan Tran L. 2020. Heat sensing and lipid reprograming as a signaling switch for heat stress responses in wheat. *Plant and Cell Physiology* **61**: 1399–1407.

Bahar NHA, Hayes L, Scafaro AP, Atkin OK, Evans JR. 2018. Mesophyll conductance does not contribute to greater photosynthetic rate per unit nitrogen in temperate compared with tropical evergreen wet-forest tree leaves. *New Phytologist* **218**: 492–505.

Ball JT, Woodrow IE, Berry JA. 1987. A model predicting stomatal conductance and its contribution to the control of photosynthesis under different environmental conditions. In: Biggins J, eds. *Progress in Photosynthesis Research*, 221–224.

Barbour MM, McDowell NG, Tcherkez G, Bickford CP, Hanson DT. 2007. A new measurement technique reveals rapid post-illumination changes in the carbon isotope composition of leaf-respired CO_2. *Plant, Cell & Environment* **30**: 469–482.

Battaglia M, Beadle C, Loughhead S. 1996. Photosynthetic temperature responses of *Eucalyptus globulus* and *Eucalyptus nitens*. *Tree Physiology* **16**: 81–89.

Bernacchi CJ, Pimentel SE, Portis AR, Long SP. 2001. Improved temperature response functions for models of Rubisco-limited photosynthesis. *Plant, Cell & Environment* **24**: 253–259.

Bernacchi CJ, Portis AR, Nakano H, von Caemmerer S, Long SP. 2002. Temperature response of mesophyll conductance. Implications for the determination of Rubisco enzyme kinetics and for limitations to photosynthesis in vivo. *Plant Physiology* **130**: 1992–1998.

Burnett AC, Davidson KJ, Serbin SP, Rogers A. 2019. The “one-point method” for estimating maximum carboxylationcapacity of photosynthesis: A cautionary tale. *Plant, Cell & Environment* **42**: 2472–2481.

Carriquí M, Roig-Oliver M, Brodribb TJ, Coopman R, Gill W, Mark K,

Niinemets Ü, Perera-Castro1 AV, Ribas-Carbó M, Sack L, Tosens T, Waite M, Flexas J. 2019. Anatomical constraints to nonstomatal diffusion conductance and photosynthesis in lycophytes and bryophytes. *New Phytologist* **222**: 1256–1270.

Carriquí M, Nadal M, Clemente-Moreno MJ, Gago J, Miedes E, Flexas J. 2020. Cell wall composition strongly influences mesophyll conductance in gymnosperms. *The Plant Journal* **103**: 1372–1385.

Carriquí M, Nadal M, Flexas J. 2021. Acclimation of mesophyll conductance and anatomy to light during leaf aging in *Arabidopsis thaliana*. *Physiologia Plantarum* **172**: 1894–1907.

Dai Y, Zeng X, Dickinson RE, Baker I, Bonan GB, Bosilovich MG, Denning AS, Dirmeyer PA, Houser PR, Niu G, Oleson KW, Schlosser CA, Yang ZL. 2003. The common land model. *Bulletin of the American Meteorological Society* **84**: 1013-1023.

Dreyer E, Montpied P, Dauder FA, Masson F. 2001. Temperature response of leaf photosynthetic capacity in seedlings from seven temperate tree species. *Tree Physiology* **21**: 223–232.

Evans J, Sharkey TD, Berry JA, Farquhar GD. 1986. Carbon isotope discrimination measured concurrently with gas exchange to investigate CO_2 diffusion in leaves of higher plants. *Australian Journal of Plant Physiology* **13**: 281–92.

Evans JR, von Caemmerer S. 2013. Temperature response of carbon isotope discrimination and mesophyll conductance in tobacco. *Plant, Cell & Environment* **36**: 745–756.

Evans JR. 2021. Mesophyll conductance: walls, membranes and spatial complexity. *New Phytologist* **229**: 1864–1876.

Farquhar GD, von Caemmerer S, Ball JA. 1980. A biochemical model of photosynthetic CO_2 assimilation in leaves of C_3 species. *Planta* **149**: 78–90.

Flexas J, Diaz-Espejo A, Galmés J, Kaldenhoff R, Medrano H, Ribas-Carbo

M. 2007. Rapid variations of mesophyll conductance in response to changes in CO_2 concentration around leaves**.** *Plant, Cell & Environment* **30:** 1284–1298

Flexas J, Barbour MM, Brendel O, Cabrera HM, Carriquí M, Díaz-Espejo A, Douthe C, Dreyer E, Ferrio JP, Gago J, Gallé A, GalmésJ, Kodama N, Medrano H, Niinemets Ü, Peguero-Pina JJ, Pou A, Ribas-Carbó M, Tomás M, Tosens T, Warren CR. 2012. Mesophyll diffusion conductance to CO_2: an unappreciated central player in photosynthesis. *Plant Science* **193**: 70–84.

Flexas J, Scoffoni C, Gago J, Sack L. 2013. Leaf mesophyll conductance and leaf hydraulic conductance: an introduction to their measurement and coordination. *Journal of Experimental Botany* **64**: 3965–3981.

Gago J, Carriquí M, Nadal M, Clemente-Moreno MJ, Coopman RE, Fernie AR, Flexas J. 2019. Photosynthesis optimized across land plant phylogeny. *Trends in Plant Science* **24**: 947-958.

Groszmann M, Osborn HL, Evans JP. 2017. Carbon dioxide and water transport through plant aquaporins. *Plant, Cell & Environment* **40**: 938–961.

Rogers A, Medlyn BE, Dukes JS, Bonan G, von Caemmerer S, Dietze MC, Kattge J, Leakey A, Mercado LM, Niinemets Ü, Prentice IC, Serbin SP, Sitch S, Way DA, Zaehle S. 2017. A roadmap for improving the representation of photosynthesis in Earth system models. *New Phytologist* **213**: 22–42.

Gu L, Pallardy SG, Tu K, Law BE, Wullschleger SD. 2010. Reliable estimation of biochemical parameters from C_3 leaf photosynthesis-intercellular carbon dioxide response curves. *Plant, Cell & Environment* **33**: 1852–1874.

Gunderson CA, O'Hara KH, Campion CM, Walker AV, Edwards NT. 2009. Thermal plasticity of photosynthesis: the role of acclimation in forest responses to a warming climate. *Global Change Biology* **16**: 2272–2286.

Han T, Zhu G, Ma J, Wang S, Zhang K, Liu X, Ma T, Shang S, Huang C. 2020. Sensitivity analysis and estimation using a hierarchical Bayesian method for the

parameters of the FvCB biochemical photosynthetic model. *Photosynthesis Research* **143**: 45–66.

Harley PC, Tenhunen JD. 1991. Modeling the photosynthetic response of C_3 leaves to environmental factors. *Modeling crop photosynthesis—from biochemistry to canopy* **19**: 17–39.

Harley PC, Loreto F, Di Marco G, Sharkey TD. 1992. Theoretical considerations when estimating the mesophyll conductance to CO_2 flux by analysis of the response of photosynthesis to CO_2. *Plant Physiology* **98**: 1429–1436.

Iqbal WA, Miller IG, Moore RL, Hope IJ, Cowan-Turner D, Kapralov MV. 2021. Rubisco substitutions predicted to enhance crop performance through carbon uptake modeling. *Journal of Experimental Botany* https://doi.org/10.1093/jxb/erab278.

Knauer J, Zaehle S, De Kauwe MG, Bahar NHA, Evans JR, Medlyn BE, Reichstein M, Werner C. 2019. Effects of mesophyll conductance on vegetation responses to elevated CO_2 concentrations in a land surface model. *Global Change Biology* **25**: 1820–1838.

Knauer J, Zaehle S, De Kauwe MG, Haverd V, Reichstein M, Sun Y. 2020. Mesophyll conductance in land surface models: effects on photosynthesis and transpiration. *The Plant Journal* **101**: 858–873.

Kumarathunge DP, Medlyn BE, Drake JE, Tjoelker MG, Aspinwall MJ, Battaglia M, Cano FJ, Carter KR, Cavaleri MA, Cernusak LA, et al. 2019. Acclimation and adaptation components of the temperature dependence of plant photosynthesis at the global scale. *New phytologist* **222**: 768–784.

Leuning R. 1995. A critical appraisal of a combined stomatal-photosynthesis model for C_3 plants. *Plant, Cell & Environment* **18**: 339–355.

Li Y, Song X, Li S, Salter WT, Barbour MM. 2020. The role of leaf water potential in the temperature response of mesophyll conductance. *New phytologist* **225:** 1193–1205.

Medlyn B.E, Ellsworth D, Forstreuter M, Harley PC, Kirschbaum MUF, Le

Roux X, Montpied P, Strassemeyer J, Walcroft A, Wang K, Loustau D. 2002. Temperature response of parameters of a biochemically based model of photosynthesis. II. A review of experimental data. *Plant, Cell & Environment* **25**: 1167–1179.

Manter DK, Kerrigan J. 2004. A/C_i curve analysis across a range of woody plant species: influence of regression analysis parameters and mesophyll conductance. *Journal of Experimental Botany* **55:** 2581–2588.

Momayyezi M, McKown AD, Bell SCS, Guy RD. 2020. Emerging roles for carbonic anhydrase in mesophyll conductance and photosynthesis. *The Plant Journal* **101**: 831-844.

Niinemets Ü, Díaz-Espejo A, Flexas J, Galmés J, Warren CR. 2009. Importanceof mesophyll diffusion conductance in estimation of plant photosynthesis inthe field. *Journal of Experimental Botany* **60**: 2271–2282.

Niu Y, Xiang Y. 2018. An overview of biomembrane functions in plant responses to high-temperature stress. *Frontiers in Plant Science* **9**, 915.

Otto B, Uehlein N, Sdorra S, Fischer M, Ayaz M, Belastegui-Macadam X, … Kaldenhoff R. 2010. Aquaporin tetramer composition modifies the function of tobacco aquaporins. *Journal of Biological Chemistry* **285**: 31253–31260.

Pons TL, Flexas J, von Caemmerer S, Evans JR, Genty B, Ribas-Carbo M, Brugnoli E. 2009. Estimating mesophyll conductance to CO_2: methodology, potential errors, and recommendations. *Journal of Experimental Botany* **60**: 2217–2234.

Sall T, Pettersson P. 1994. A model of photosynthetic acclimation as a special case of reaction norms. *Journal of Theoretical Biology* **166**: 1–8.

Salvucci ME, Crafts-Brandner SJ. 2004. Relationship between the heat tolerance of photosynthesis and the thermal stability of Rubisco activase in plants from contrasting thermal environments. *Plant Physiology* **134**: 1460–1470.

Sellers PJ, Randall DA, Collatz GJ, Berry JA, Field CB, Dazlich DA, Zhang C, Collelo GD, Bounoua L. 1996. A revised land surface parameterization (SiB2)

for atmospheric GCMS. Part I: model formulation. *Journal of Climate* **9**: 676–705.

Scafaro AP, von Caemmerer S, Evans JR, Atwell BJ. 2011. Temperature response of mesophyll conductance in cultivated and wild Oryza species with contrasting mesophyll cell wall thickness. *Plant, Cell & Environment* **34**: 1999–2008.

Sharkey TD, Bernacchi CJ, Farquhar GD, Singsaas EL. 2007. Fitting photosynthetic carbon dioxide response curves for C_3 leaves. *Plant, Cell & Environment* **30**: 1035–1040.

Silim SN, Ryan N, Kubien D. 2010. Temperature response of photosynthesis and respiration in *Populus balsamifera* L.: acclimation versus adaption. *Photosynthesis Research* **104**: 19–30.

Shrestha A, Song X, Barbour MM. 2019. The temperature response of mesophyll conductance, and its component conductances, varies between species and genotypes. *Photosynthesis Research* **141**: 65–82.

Sun Y, Gu L, Dickinson RE, Pallardy SG, Baker J, Cao Y, DaMatta FM, Dong X, Ellsworth D, Van Goethem D, Jensen AM, Law BE, Loos R, Martins SC, Norby RJ, Warren J, Weston D, Winter K. 2014. Asymmetrical effects of mesophyll conductance on fundamental photosynthetic parameters and their relationships estimated from leaf gas exchange measurements. *Plant, Cell & Environment* **37**: 978–994.

Tomas M, Flexas J, Copolovici L, Galmes J, Hallik L, Medrano H, Ribas-Carbo M, Tosens T, Vislap V, Niinemets Ü. 2013. Importance of leaf anatomy in determining mesophyll diffusion conductance to CO_2 across species: quantitative limitations and scaling up by models. *Journal of Experimental Botany* **64**: 2269–2281.

Tosens T, Niinemets Ü, Vislap V, Eichelmann H, Castro Diez P. 2012. Developmental changes in mesophyll diffusion conductance and photosynthetic capacity under different light and water availabilities in *Populus tremula*: how structure constrains function. *Plant, Cell & Environment* **35**: 839–856.

Tosens T,LaanistoL. 2018. Mesophyll conductance and accurate photosynthetic carbon gain calculations. *Journal of Experimental Botany* **69**: 5315–5318.

Triandafillou CG, Katanski CD, Dinner AR, Drummond DA. 2020. Transient intracellular acidification regulates the core transcriptional heat shock response. *Elife* **9**: e54880.

von Caemmerer S, Farquhar G, Berry J. 2009. Biochemical model of C_3 photosynthesis. In: Laisk, A., Nedbal, L., Govindjee, eds. *Photosynthesis in silico: Understanding complexity from molecules to ecosystems.* Springer Netherlands, Dordrecht, pp. 209–230.

von Caemmerer S. 2013. Steady-state models of photosynthesis. *Plant, Cell & Environment* **36**: 1617–1630.

von Caemmerer S, Evans JR. 2015. Temperature responses of mesophyll conductance differ greatly between species. *Plant, Cell & Environment* **38**: 629–637.

von Caemmerer, S., 2020. Rubisco carboxylase/oxygenase: From the enzyme to the globe: A gas exchange perspective. *Journal of Plant Physiology* **252**: 153240.

Warren CR, Dreyer E. 2006. Temperature response of photosynthesis and internal conductance to CO_2: results from two independent approaches. *Journal of Experimental Botany* **57**: 3057–3067.

Wang XL, Cao ZL, He RX, Chen S. 2016. Research on the stability of pH values, temperatures and storage factors of carbonic anhydrase in *Pinus yunnanensis* needles. *Journal of Yunnan University* **38**: 501–506. (In Chinese with English abstract)

Xiao, Y., Sloan, J., Hepworth, C., Osborne, C.P., Fleming, A.J., Chen, X., Zhu, X.G., 2021. Estimating uncertainty: A Bayesian approach to modelling photosynthesis in C_3 leaves. *Plant, Cell & Environment* **44**: 1436–1450.

Xu L, Badocchi D. 2003. Seasonal trends in photosynthetic parameters and stomatal conductance of blue oak (*Quercus douglasii*) under prolonged summer. *Tree Physiology* **23**: 865–877.

Xu Y, Shang B, Feng Z, Tarvainen L. 2020. Effect of elevated ozone, nitrogen availability and mesophyll conductance on the temperature responses of leaf photosynthetic parameters in poplar. *Tree Physiology* **40**: 484–497.

Xue W, Otieno D, Ko J, Werner C, Tenhunen J. 2016. Conditional variations in temperature response of photosynthesis, mesophyll and stomatal control of water use in rice and winter wheat. *Field Crops Research* **199**: 77–88.

Xue W, Ko J, Werner C, Tenhunen J. 2017. A spatially hierarchical integration of close-range remote sensing, leaf structure and physiology assists in diagnosing spatiotemporal dimensions of field-scale ecosystem photosynthetic productivity. *Agricultural and Forest Meteorology* **247**: 503–519.

Yin X, Struik PC. 2009. Theoretical reconsiderations when estimating the mesophyll conductance to CO_2 diffusion in leaves of C_3 plants by analysis of combined gas exchange and chlorophyll fluorescence measurements. *Plant, Cell & Environment* **32**: 1513–1524.

Zhao M., Tan H-T, Scharwies J, Levin K, Evans JR, Tyerman SD. 2017. Association between water and carbon dioxide transport in leaf plasma membranes: assessing the role of aquaporins. *Plant, Cell & Environment* **40**: 789–801.

Zheng SZ, Liu YL, Li B, Shang ZL, Zhou RG, Sun DY. 2012. Phosphoinositide-specific phospholipase C9 is involved in the thermotolerance of Arabidopsis. *The Plant Journal* **69**: 689–700.

Zhu GF, Li X, Su YH, Lu L, Huang CL. 2011. Seasonal fluctuations and temperature dependence in photosynthetic parameters and stomatal conductance at the leaf scale of *Populus euphratica* Oliv. *Tree physiology* **31**:178–195.

Supporting Information

Additional supporting information may be found in the online version of this article:

Fig. S1 The temperature response curves of V_{cmax}.

Fig. S2 The temperature response curves of J_{max}.

Fig. S3 The temperature response curves of g_m.

Fig. S4 Temperature response curves of the net assimilation rate under ambient CO_2 concentration (400–450 ppm) and high radiation derived from field measurements and predictions.

Fig. S5 Temperature response curves of the net assimilation rate under ambient CO_2 concentration (600–630 ppm) and high radiation derived from field measurements and predictions.

Fig. S6 Comparisons in diurnal photosynthesis rate between field observations and predictions.

Fig. S7 Comparisons in diurnal transpiration rate between field observations and predictions.

Fig. S8 Comparisons in diurnal stomatal conductance between field observations and predictions.

Fig. S9 Comparisons in diurnal A_n at PAR greater than 1500 μmol m^{-2} s^{-1} and across a wide range of leaf temperatures between observations and predictions using the g_m infinite model and the g_m finite model that is forced by the parameterization scheme SB_FA.

Fig. S10 Statistical relationships for photosynthesis optimal temperature and the ratio of the maximum carboxylation rate to the maximum electron transport rate (JVr) (a), T_{optA}–$g_{m_F,25}$ (b), and T_{optA}–activation term of g_{m_F} (ΔH_a) (c).

Table S1 Temperature response characteristic parameters of V_{cmax}.

Table S2 Temperature response characteristic parameters of J_{max}.

Table S3 Temperature response characteristic parameters of g_m.

Methods S1 The explicit clarity on the parameter values assumed for each parameter estimation method

Methods S2

Methods S3

Methods S4

Methods S5

Methods S6

Methods S7